

Article

# Transition Metal-Modified Zirconium Phosphate Electrocatalysts for the Oxygen Evolution Reaction

Joel Sanchez <sup>1</sup>, Mario V. Ramos-Garcés <sup>2</sup>, Ieva Narkeviciute <sup>1</sup>, Jorge L. Colón <sup>2,\*</sup>  
and Thomas F. Jaramillo <sup>2,\*</sup>

<sup>1</sup> Department of Chemical Engineering, Stanford University, Stanford, CA 94305, USA; joelsan@stanford.edu (J.S.); ieva@stanford.edu (I.N.)

<sup>2</sup> Department of Chemistry, University of Puerto Rico-Río Piedras Campus, P.O. Box 70377, San Juan, PR 00936-8377, USA; mario.ramos1@upr.edu

\* Correspondence: jorge.colon10@upr.edu (J.L.C.); jaramillo@stanford.edu (T.F.J.); Tel.: +1-787-402-2015 (J.L.C.); +1-650-353-1984 (T.F.J.)

Academic Editor: Monica Pica

Received: 1 March 2017; Accepted: 20 April 2017; Published: 1 May 2017

**Abstract:** Zirconium phosphate (ZrP), an inorganic layered nanomaterial, is currently being investigated as a catalyst support for transition metal-based electrocatalysts for the oxygen evolution reaction (OER). Two metal-modified ZrP catalyst systems were synthesized: metal-intercalated ZrP and metal-adsorbed ZrP, each involving Fe(II), Fe(III), Co(II), and Ni(II) cations. Fourier transform infrared spectroscopy, X-ray powder diffraction, thermogravimetric analysis, and X-ray photoelectron spectroscopy were used to characterize the composite materials and confirm the incorporation of the metal cations either between the layers or on the surface of ZrP. Both types of metal-modified systems were examined for their catalytic activity for the OER in 0.1 M KOH solution. All metal-modified ZrP systems were active for the OER. Trends in activity are discussed as a function of the molar ratio in relation to the two types of catalyst systems, resulting in overpotentials for metal-adsorbed ZrP catalysts that were less than, or equal to, their metal-intercalated counterparts.

**Keywords:** zirconium phosphate; intercalation; ion exchange; catalyst support; oxygen evolution reaction; electrocatalysis; water oxidation

## 1. Introduction

The renewable, sustainable production of hydrogen could have many benefits, displacing the conventional fossil-based processes for its production and use in the fuels and chemical industry, and potentially serving as an alternative energy vector given its high gravimetric energy density and modularity of use [1]. Conventional hydrogen is produced through steam methane reforming, but hydrogen produced by water electrolysis has the potential to be CO<sub>2</sub>-emission free if the energy required is provided by renewable energy sources. Technological improvements will be needed for the cost-effectiveness of electrolysis to compete with current methods of hydrogen production [2,3]. Water electrolysis is the decomposition of water through two half-reactions of water splitting, the oxygen evolution reaction (OER) and the hydrogen evolution reaction (HER). The OER is important for many renewable energy conversion technologies, such as photoelectrochemical cells, regenerative fuel cells, and electrolyzers [1,4,5]. In acid systems, Ir and Ru-based oxides are common catalysts for the OER, while in alkaline environments non-precious transition metal oxides based on Ni, Fe, and Co are commonly employed [6–10]. In all cases, OER catalysts suffer from considerable overpotential losses, limiting the efficiency of hydrogen generation by water electrolysis processes [11].

To overcome these challenges and thus to facilitate the economic viability of electrolysis, the efficiencies of electrolyzer systems must be improved by addressing the kinetic overpotential

losses associated with turning over the OER and, ideally, using catalysts based on Earth-abundant elements. Recent studies have focused on reducing the amount of precious metals in OER catalysis, using more Earth-abundant transition metals in their oxide and/or hydroxide form to catalyze the reaction [12–14]. However, as reported by recent experimental benchmarking efforts and supported by theoretical calculations, the overpotentials of state-of-the-art catalysts have plateaued close to the theoretical minimum overpotential for the OER, predicted for conventional materials, including those based on precious metals [15,16]. Significant research has been conducted to improve electrocatalysts through a number of general strategies, including increasing the number of active sites, increasing the intrinsic activity of each active site, and/or supporting the active material onto supports that engender improved performance [17–21]. In particular, catalyst supports have shown to play an important role in the performance and stability of catalysts for many different reactions [22–24].

In this study, the use of the zirconium phosphate (ZrP) type of layered inorganic compounds, as a support for water oxidation catalysts, is examined. The most extensively studied phase of ZrP is zirconium bis(monohydrogen orthophosphate) monohydrate ( $\text{Zr}(\text{HPO}_4)_2 \cdot \text{H}_2\text{O}$ ,  $\alpha$ -ZrP), a layered compound with an interlayer distance of 7.6 Å and a layer thickness of 6.6 Å (Figure 1A) [25].  $\alpha$ -ZrP has a structure in which the Zr atoms in each layer align nearly to a plane with bridging phosphate groups 5.3 Å apart, which are located alternately above and below the metal atom plane [25]. Three oxygen atoms of the phosphate group bond to three different  $\text{Zr}^{4+}$  ions; six O atoms from different phosphate groups coordinate the Zr atoms forming an octahedral coordination symmetry around each Zr atom. These bridging phosphate groups provide an ion exchange site where the proton can be exchanged with cations and other species. The above-mentioned structure of  $\alpha$ -ZrP creates a small molecule-sized cavity in the interlayer region with a diameter of 2.61 Å, which is occupied by a water molecule [25]. For  $\alpha$ -ZrP, the direct intercalation of small cations is possible if they are smaller than 2.61 Å, but for larger cations and molecules, intercalation is not significant and/or these species are exchanged at very slow rates [26–28]. A direct intercalation method that can circumvent this problem involves a highly hydrated phase of zirconium phosphate,  $\text{Zr}(\text{HPO}_4)_2 \cdot 6\text{H}_2\text{O}$ ,  $\theta$ -ZrP [29].  $\theta$ -ZrP maintains the  $\alpha$ -ZrP-type layered structure (Figure 1B), but has an interlayer distance of 10.4 Å and has six water molecules per formula unit, in contrast with  $\alpha$ -ZrP that only has one [30]. Figure 1C shows transmission electron micrographs of  $\alpha$ -ZrP nanoparticles with the characteristic hexagonal nano-platelet structure with an average diameter and thickness of ~140 and ~15 nm, respectively.

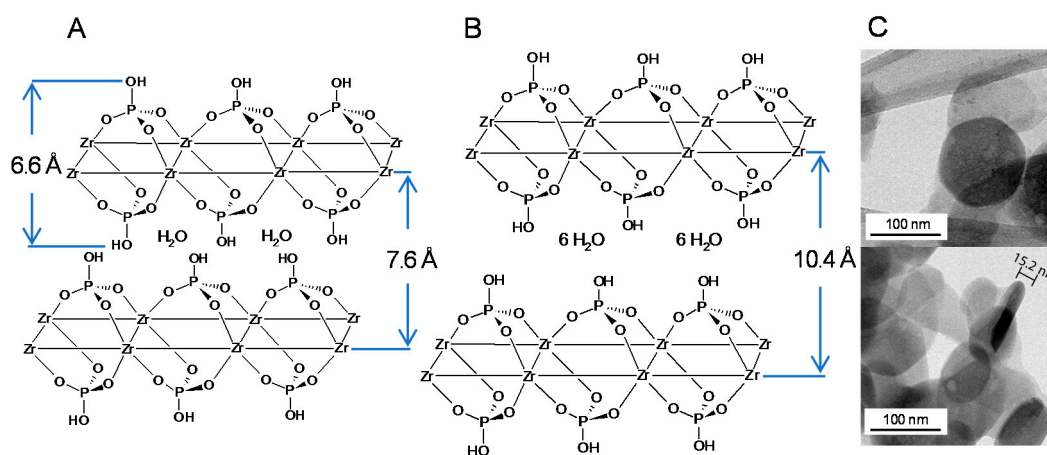


**Figure 1.** (A) The structure of  $\alpha$ -ZrP; (B) the structure of  $\theta$ -ZrP; and (C) TEM micrographs of  $\alpha$ -ZrP nanoparticles where the top image shows the characteristic hexagonal shape and the bottom image shows the thickness of an  $\alpha$ -ZrP nanoparticle.

$\theta$ -ZrP can be directly ion-exchanged with large metal complexes, producing intercalated phases useful for artificial photosynthesis schemes, amperometric biosensors, vapochromic materials, catalysis,

and drug delivery applications [31–35]. Herein, the layered structure of ZrP is leveraged to support active catalysts for the OER through the ion exchange of transition metal cations. Intercalation of various metals of divalent and trivalent character (Fe(II), Fe(III), Co(II), Ni(II)) were performed on  $\theta$ -ZrP at various metal to  $\theta$ -ZrP molar ratios. For comparison, we also investigate the same transition metal systems adsorbed onto the outer surface of  $\alpha$ -ZrP, achieved using a similar synthesis procedure, however, due to the much tighter interlayer spacing of  $\alpha$ -ZrP compared to  $\theta$ -ZrP, intercalation is not readily achieved. These two types of metal-modified ZrP, metal-intercalated ZrP and metal-adsorbed ZrP, are studied herein for their physical and chemical properties, including as OER catalysts. These oxygen evolution electrocatalyst materials were thoroughly characterized by Fourier transform infrared spectroscopy (FTIR), thermogravimetric analysis (TGA), X-ray powder diffraction (XRPD), X-ray photoelectron spectroscopy (XPS), and cyclic voltammetry. For the catalyst systems studied here in alkaline electrolyte, we generally find that the metal-adsorbed ZrP catalysts are more active than their intercalated counterparts, e.g., a metal-adsorbed Fe(II)-ZrP at a 10:1 Fe(II):ZrP molar ratio that requires an overpotential of 490 mV at 10 mA/cm<sup>2</sup>, while its metal-intercalated counterpart at the same molar ratio requires an overpotential of 520 mV at 10 mA/cm<sup>2</sup>.

## 2. Results and Discussion

### 2.1. FTIR and TGA Analysis of Interlayer and Surface Modification of ZrP

Each metal-modified (metal-intercalated and metal-adsorbed) ZrP sample was created through suspensions of  $\theta$ -ZrP and  $\alpha$ -ZrP in deionized water mixed with Fe(II), Fe(III), Co(II), and Ni(II) metal salts. The loading level was controlled by varying the metal:ZrP (M:ZrP) molar ratio used in the suspension over a wide range (1:20–10:1), and the materials are referenced according to this concentration ratio throughout the article. Figure 2 shows the IR spectra of pure  $\alpha$ -ZrP, metal-intercalated ZrP, and metal-adsorbed ZrP. The four characteristic  $\alpha$ -ZrP bands associated with lattice water were observed in the pure material. Three of them are sharp bands at 3592 cm<sup>-1</sup>, 3510 cm<sup>-1</sup>, and 1616 cm<sup>-1</sup>, while the fourth is a broad band at ca. 3141 cm<sup>-1</sup> [36]. For the metal-intercalated samples, the two sharp bands at 3592 cm<sup>-1</sup> and 3510 cm<sup>-1</sup> are not observed, while the other two bands have reduced intensity compared to pure  $\alpha$ -ZrP. When intercalation occurs, the intercalant species will displace interlayer water molecules. For this reason, bands associated with these water vibrational modes will show reduced relative intensity in the intercalated materials; therefore, the IR data shown in Figure 2A is consistent with intercalation of the metal species into ZrP interlayers, as also indicated by the XRPD data (vide infra). In contrast, metal-adsorbed samples show very similar spectra to that of  $\alpha$ -ZrP, with the sharp bands present at 3592 cm<sup>-1</sup> and 3510 cm<sup>-1</sup>, indicating negligible intercalation, as expected.

The characteristic orthophosphate group vibrations of ZrP are observed in the region of ca. 1057–966 cm<sup>-1</sup> for all samples [36]. Metal-intercalated samples show a diminished relative intensity of the shoulder at the bottom left part of the orthophosphate group vibrations at ca. 1050 cm<sup>-1</sup>, attributed to the vibration of the exchangeable proton of the phosphate group, which is lost when the proton is exchanged by intercalation via ion exchange with other species [36]. This is observed for all metal-intercalated systems, another indication of successful intercalation. For metal-adsorbed samples, this vibration is still present indicating, once again, that no intercalation is observed and, for clarity, Figure S1 shows the characteristic 3592 and 3510 cm<sup>-1</sup> peaks for adsorbed Fe(III)-ZrP.

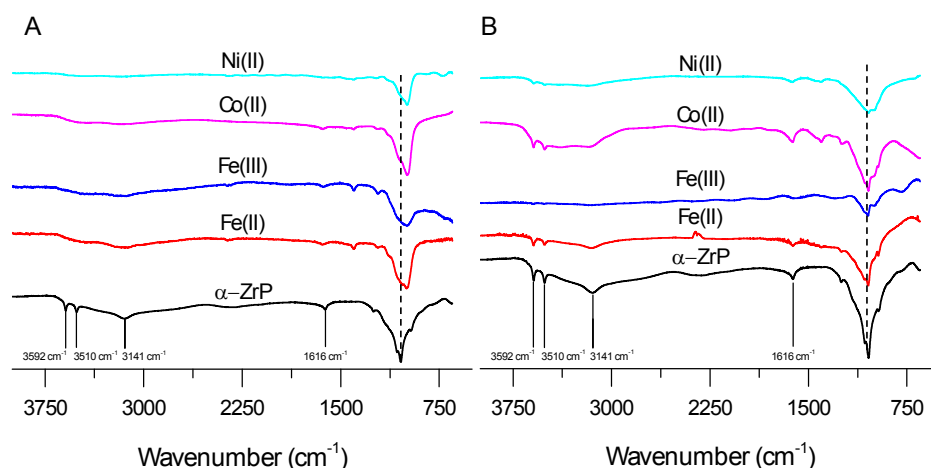


**Figure 2.** FTIR spectra of (A) intercalated and (B) adsorbed Fe(II), Fe(III), Co(II), and Ni(II) at 10:1 M:ZrP ratio.

TGA was performed to further corroborate that intercalation had occurred for the metal-intercalated systems and that the metal-adsorbed catalyst had retained  $\alpha$ -ZrP characteristics. In the case of pure  $\alpha$ -ZrP (Figure 3) two weight losses are observed, dehydration of water within the interlayer below 150 °C, followed by condensation to zirconium pyrophosphate at ~500 °C, leading to a total weight loss of ~13%, in agreement to previous literature results [37]. All metal-intercalated systems (Figure 3A) showed significant deviation from pure  $\alpha$ -ZrP, especially within the temperature range that pyrophosphate is formed. Based on thermograms for pure  $\alpha$ -ZrP as a reference, two regions are observed for Fe(II)-intercalated systems—the dehydration of interlayer water corresponding to an 8.7% weight loss at 76 °C, followed by a gradual shoulder decrease in weight loss of 4% up to 200 °C. Fe(III)-intercalated systems show a 5% weight loss followed by a 3% weight loss for interlayer water dehydration and phosphate condensation, respectively. Similar results were found to those observed in previous studies for TGA thermograms involving intercalated Co(II) and Ni(II) ZrP systems [38]. Both Co(II) and Ni(II)-ZrP lose interlayer water below 150 °C for weight losses of ~12% and 10%, respectively. Since divalent and trivalent transition metal cations are highly hydrated in their intercalated form [39]; previously-reported reflectance and Extended X-ray Absorption Fine Structure (EXAFS) spectra show that Co(II)- and Ni(II)-exchanged ZrP at room temperature are octahedrally coordinated with water [40,41]. The 3% weight loss between 200 and 300 °C for Co(II)-ZrP corresponds to loss of metal coordinated waters, and the loss of structural water due to decomposition of the phosphate groups is evident between temperatures of 350 to 500 °C [38]. For Ni(II)-intercalated samples, the loss of coordinated waters between 250 °C and 300 °C results in a 5% weight loss, and decomposition of the phosphate groups to form pyrophosphate occurs between 350 °C and 500 °C [38,42]. Ni(II)-ZrP samples are more stable than Co(II)-ZrP, as expected due to their higher ligand field stabilization energy [43]. Conversely, for all adsorbed cases (Figure 3B), their respective thermograms were similar to  $\alpha$ -ZrP indicating that no major modification of the interlayer had occurred except for a reduction in weight loss for pyrophosphate, showing that the surface phosphates had undergone modification by the metal cations. All FTIR spectra and TGA thermograms are within expected results for our ZrP systems and further substantiate that intercalated and adsorbed systems were created as planned.

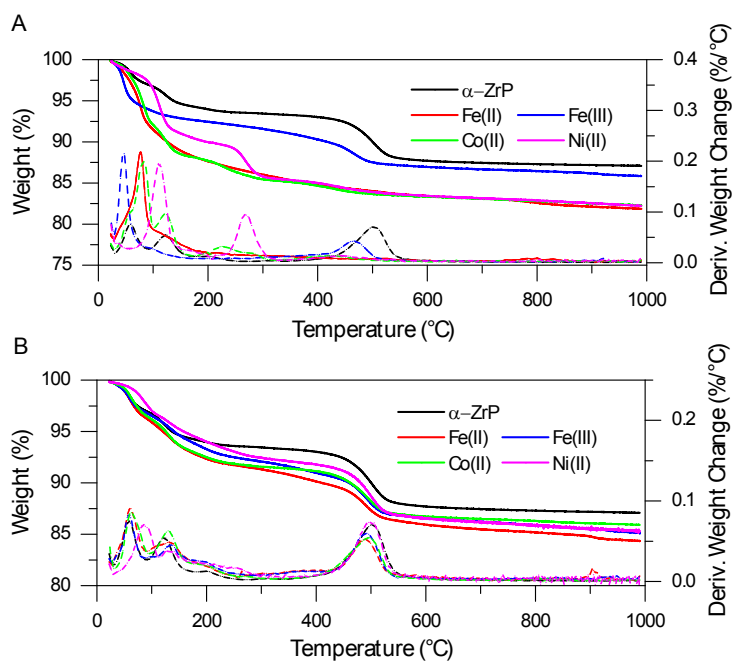


**Figure 3.** TGA thermograms of (A) intercalated and (B) adsorbed Fe(II), Fe(III), Co(II), and Ni(II) at a 10:1 M:ZrP ratio. Solid lines and dashed lines correspond to normalized weight and the first derivative of weight change with respect to temperature, respectively.

## 2.2. XRPD Interlayer Expansion Analysis of Metal-Modified ZrP

To assess possible interlayer expansion of ZrP sheets as a function of transition metal and cation valence, X-ray powder diffraction (XRPD) measurements were performed for dried metal-modified ZrP systems. If pure  $\theta$ -ZrP is dried, dehydration converts it to  $\alpha$ -ZrP; therefore, all samples are referenced to the  $\alpha$ -ZrP (002) diffraction peak at  $2\theta = 11.5^\circ$ , corresponding to an interlayer distance of 7.6 Å [44]. As described in the literature, an intercalation reaction can occur in a stepwise fashion depending on the intercalation energy threshold of the intercalants [45]. During this process, one of three possible patterns can be observed by XRPD for metal-modified ZrP; either (i) a pattern with a peak corresponding to a larger interlayer spacing at lower  $2\theta$  values than  $11.5^\circ$  indicating that metal cations were introduced into the interlayer; (ii) a pattern with two distinct peaks—one at approximately  $2\theta = 11.5^\circ$  and one that appears at lower  $2\theta$  values than the reference peak indicating that a mixed phase is present; and (iii) a pattern with no change in the reference peak, indicating that the cation species is adsorbed on the outer surface of the layered structure rather than being intercalated [44]. Below, the XRPD analysis for all metal-modified ZrP systems is presented.

Figure 4A shows the XRPD of pure  $\alpha$ -ZrP and metal-intercalated ZrP for Fe(II), Fe(III), Co(II), and Ni(II), at M:ZrP molar ratios ranging from 1:20 to 10:1. A stepwise process is expected as a function of intercalant solution molarity; the intercalation reaction initiates from the edges of the particle and proceeds by diffusion of the metal cations towards the interior of the interlayer sheets [37]. The diffraction patterns for all four metal cation systems show a shift of the first diffraction peak towards lower  $2\theta$  values compared to the (002) peak of pure  $\alpha$ -ZrP, indicating that new intercalated phases with expanded interlayer distance ( $>7.6$  Å) were obtained, even for the lowest M:ZrP molar ratio of 1:20. Increasing the M:ZrP molar ratios to 1:10 and 1:3 results in further broadening and shifting of the peak across all samples, indicating a more mixed phase is present, and that the layered structure has not achieved its maximum cation loading within the interlayer. At the highest loadings (i.e., 1:1 to 10:1 molar ratios), the original peak at  $2\theta = 11.5^\circ$  has disappeared, with a new peak emerging at significantly lower values of  $2\theta$ , reaching a final value indicative of the maximum interlayer distance for that particular metal cation intercalated within ZrP. Figure S2 shows additional data regarding the

(020) and (312) reflections of these catalyst systems, further confirming that the intercalated products for the metal-intercalated systems retained the layered structure of ZrP.

As expected for an ion-exchange reaction, Figure 4B shows that intercalated samples with divalent cations (i.e., Fe(II)) underwent a much larger interlayer spacing transformation than trivalent cations (i.e., Fe(III)), with an average increase of 2.0 and 0.6 Å, respectively. During intercalation, higher valence species induce a strong electrostatic interaction with the anionic interlayers, which mitigates interlayer expansion [46]. Figure 4B also shows that, for the case of the metal-adsorbed ZrP systems, their respective interlayer spacing were unchanged and remained equal to that of  $\alpha$ -ZrP (7.6 Å) at 1:1–1:10 molar ratios, conclusively showing that, for these particular materials, the metal is adsorbed on the surface and not intercalated. Figure S3 shows the XRPD data for these systems, revealing that the adsorbed species have an identical XRPD pattern to pure  $\alpha$ -ZrP confirming that the characteristic  $\alpha$ -like layered structure is still intact for the metal-adsorbed system. As the catalysts were not processed further (e.g., with heat treatments), the form of the metal resulting on the surface of ZrP is amorphous and, as expected, no diffraction corresponding to those metals is observed by XRPD. We note that it is possible that the metal-intercalated ZrP systems might also contain adsorbed metals on their surfaces (that are also not observable by XRPD) in addition to those within the layers.

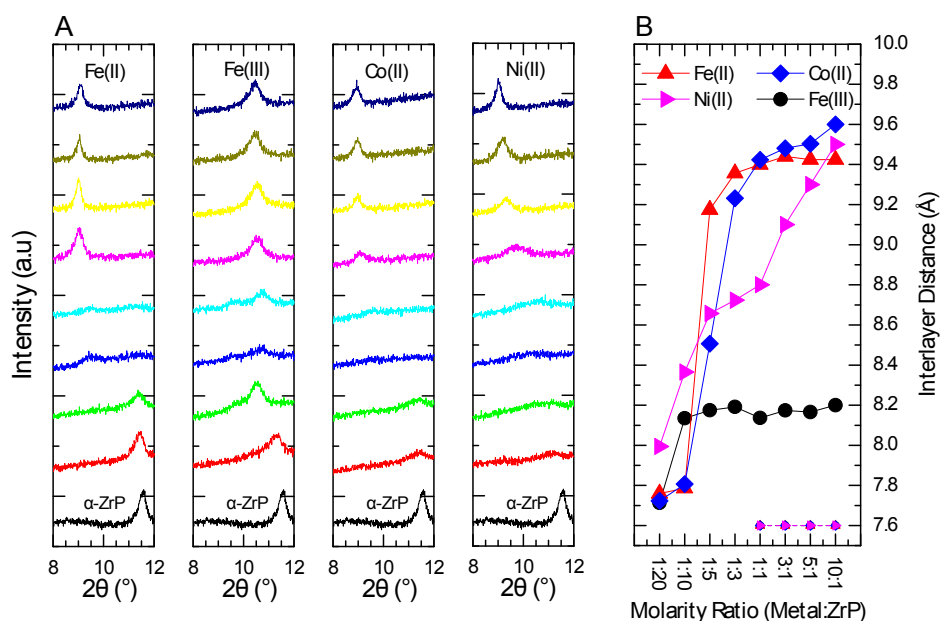


**Figure 4.** (A) XRPD patterns for Fe(II), Fe(III), Co(II), and Ni(II)-intercalated ZrP at (from top to bottom) 10:1, 5:1, 3:1, 1:1, 1:3, 1:5, 1:10, and 1:20 M:ZrP molar ratios. The bottom diffraction pattern in all frames is that of pure  $\alpha$ -ZrP. (B) Interlayer distance as a function of M:ZrP molar ratio for the various metal-intercalated ZrP materials. Metal-adsorbed systems are represented as dashed lines which have an exact interlayer spacing as pure  $\alpha$ -ZrP indicating that metal intercalation did not occur.

### 2.3. XPS Analysis of Metal Loading and Chemical Composition of Metal-Modified ZrP

To quantify the relative amounts of cations for the metal-modified ZrP systems, and to investigate the chemical nature of the metal, XPS spectra were obtained for metal-modified catalysts at 10:1 M:ZrP molar ratios for all four metals and at 1:1 to 10:1 molar ratios for the Fe(II)-ZrP system. Figure 5 shows XPS atomic concentrations of intercalated and adsorbed M(II/III):ZrP at high loadings. As expected, due to the uptake of metal cations within the much larger area of the interlayers of ZrP rather than solely on the surface in the adsorbed case, XPS high-resolution scans show that intercalated ZrP systems have higher atomic metal content when compared to adsorbed systems at similar M:ZrP ratios. As depicted in Figure 6, the characteristic peaks for Zr, P, and the respective metals were present for all samples.

The XPS spectra of Fe(II) samples in Figure 5A show the Fe 2p<sub>3/2</sub> and Fe 2p<sub>1/2</sub> peaks for the intercalated samples at 712.4 eV and 725.8 eV, respectively, and for the adsorbed samples at 713.0 eV and 726.6 eV, respectively. The peak positions of Fe(II) 2p<sub>3/2</sub> and 2p<sub>1/2</sub> peaks in oxide materials are expected at approximately 709.0 eV and 723.0 eV, respectively [47]. Figure 6A shows that for both the Fe(II)-intercalated and the Fe(II)-adsorbed systems, higher binding energies are observed, which might correspond to partial oxidation of the Fe(II) species upon ZrP incorporation due to interactions with the phosphate groups; the Fe 2p<sub>3/2</sub> peak in FePO<sub>4</sub> is expected at 712.8 eV [48]. On the other hand, the Fe(III)-intercalated sample, Figure 5A shows the Fe 2p<sub>3/2</sub> peak at 711.6 eV, which is more consistent with previously-reported values expected for Fe(III) oxides, which generally exhibit the Fe 2p<sub>3/2</sub> peak between 710.6 and 711.2 eV [47].

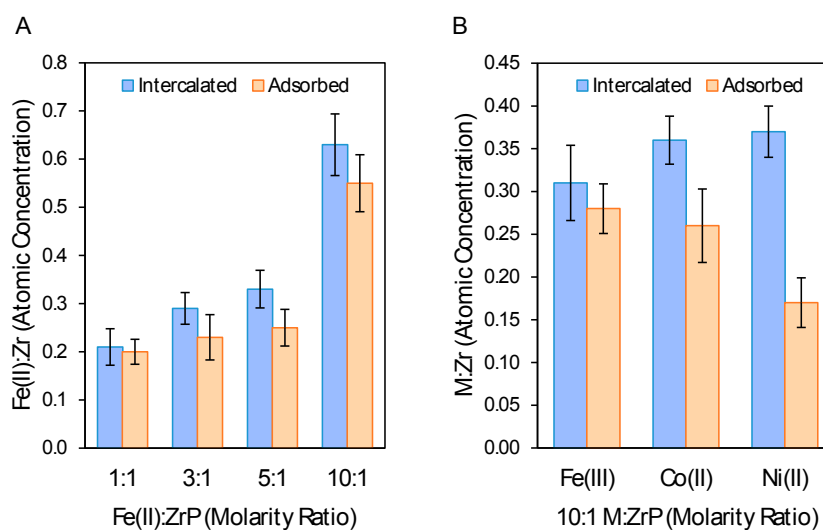


**Figure 5.** (A) Atomic concentration Fe:Zr ratios for metal-modified 1:1–10:1 Fe(II):ZrP molar ratio catalysts. (B) Atomic concentration M:Zr ratios for Fe(III), Co(II), and Ni(II) metal-modified 10:1 M:ZrP molar ratio catalysts.

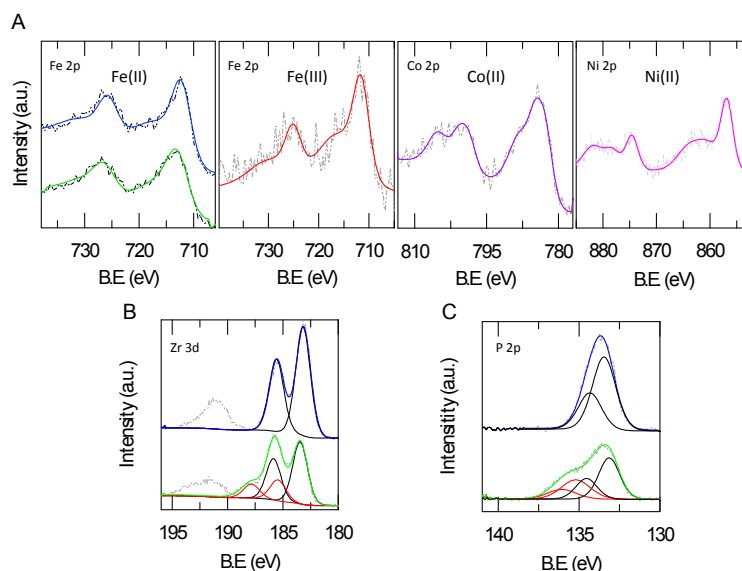
Deconvolution of the XPS spectra for Co(II) and Ni(II) is challenging due to the small shifts in the binding energy for the (II) and (III) metal oxidation states and the broad satellite peaks [49,50]. For the Co(II) sample, Figure 6A shows a Co 2p XPS spectrum with 2p<sub>3/2</sub> and 2p<sub>1/2</sub> peaks with characteristic satellite peaks, similar to those seen in other cobalt-based zirconium phosphate catalysts, but at higher binding energies, suggesting a partial oxidation of the Co species, containing both Co(II) and Co(III) characteristics [51]. For the Ni(II)-ZrP, Figure 6A shows a Ni 2p XPS spectrum with 2p<sub>3/2</sub> and 2p<sub>1/2</sub> peaks with satellite peaks, as well. The positions of the 2p<sub>3/2</sub> and 2p<sub>1/2</sub> peaks lie in between that of nickel oxide and nickel phosphate potentially elucidating that Ni cations are strongly interacting with both oxygen and phosphorus atoms in the ZrP [50,52].

Figure 6B shows the Zr 3d<sub>5/2</sub> and 3d<sub>3/2</sub> peaks and the P 2s peak for both intercalated and adsorbed samples, for the 10:1 Fe(II)-ZrP sample. In addition, Figure 6C shows the P 2p<sub>3/2</sub> and 2p<sub>1/2</sub> peaks which overlap and are, therefore, observed as a single, broad peak. For intercalated samples (blue traces), the binding energies observed for Zr and P are similar to those previously reported.

Previous reports of XPS results for modified ZrP systems have shown that intercalants can modify the polarization of both Zr and P atoms and, as a result, vary their respective binding energies when compared to pristine  $\alpha$ -ZrP [53,54]. For the adsorbed 10:1 Fe(II)-ZrP sample, two Zr species are observed, a doublet with peaks of lower intensity, but higher binding energy (red traces), and another doublet with binding energy as reported in the literature for  $\alpha$ -ZrP (black traces). The high-resolution scans for the Zr 3d region in M:Zr samples show an increase in binding energy compared to that of  $\alpha$ -ZrP, which indicates an increase in the polarization of the Zr atoms in the adsorbed samples due to interactions with the metal species. Similar results are seen for the P 2p<sub>3/2</sub> and 2p<sub>1/2</sub> binding energy

region, where the polarization also produces a shift to increased binding energy compared to the values in  $\alpha$ -ZrP. The presence of this polarization on the Zr and P atoms is more pronounced on the metal-adsorbed ZrP samples because the metal concentration on the surface of ZrP is higher than the metal-intercalated ZrP and, hence, the surface sensitivity of XPS can detect this binding energy shift.

While the XPS measurements help to inform the chemical state of the metal-modified ZrP systems, we note that changes are expected from their dry powder form to that in an electrochemical environment, held at the oxidative potentials needed for water oxidation in an alkaline solution.



**Figure 6.** (A) XPS spectra for Fe(II), Fe(III), Co(II), and Ni(II) ZrP systems. Blue and green curves in Fe(II) panel represent the 10:1 M:ZrP intercalated and adsorbed systems, respectively, while intercalated 10:1 M:ZrP systems are represented in the Fe(III), Co(II), and Ni(II) panels. (B) XPS spectra for Zr 3d and (C) P 2p where blue and green curves represent intercalated and adsorbed systems, respectively, from 10:1 Fe(II):ZrP.

#### 2.4. Electrochemical Studies of Metal-Modified ZrP

To study the electrocatalytic activity of metal-modified ZrP systems for the OER, cyclic voltammetry (CV) measurements were performed in a three-electrode rotating disk electrode (RDE) configuration with a 0.1 M KOH electrolyte. To make the working electrode, the metal-modified ZrP catalysts were mixed with carbon black in a water-based solution and deposited onto a glassy carbon disk. One figure of merit conventionally used to describe OER catalyst performance is the overpotential necessary to reach a current density of  $10 \text{ mA/cm}^2$  [15]. Figure 7A,B show cyclic voltammograms for the highest performance metal-modified ZrP system with either Fe(II) adsorbed or intercalated, while the other systems can be found in Figure S4. For reference, pure  $\alpha$ -ZrP loaded onto carbon black shows only moderate activity for the OER, unable to achieve  $10 \text{ mA/cm}^2$  even at high oxidative potentials, which is comparable to other Zr-based systems [55]. Once metal cations are ion exchanged into and/or supported onto ZrP, an active OER catalyst is produced for both metal-modified ZrP systems at various M:ZrP ratios. Adsorbed Fe(II)-ZrP shows a gradual increase in performance as the M:ZrP concentration increases and similar results are observed for the intercalated case. As shown in Figure 5, higher metal content is achieved at higher M:ZrP molar ratios for both systems; therefore, it is likely that this gradual increase in activity can be attributed to higher atomic concentrations. The adsorbed 10:1 Fe(II):ZrP molar ratio exhibits the highest OER performance of all the systems investigated herein, requiring an overpotential of 490 mV at  $10 \text{ mA/cm}^2$  with a 0.55:1 Fe:Zr atomic ratio, as determined by XPS. For comparison, the metal-intercalated equivalent system of 10:1 Fe(II):

ZrP (with a higher Fe:Zr atomic ratio of 0.63:1) requires a higher overpotential of 524 mV, suggesting that the metal intercalated within ZrP may not be electrochemically accessible for water oxidation.

Figure 7C shows electrochemical data comparing the other metal-modified ZrP systems. All metal-modified systems are catalytically active, requiring between 0.5 and 0.7 V of overpotential to reach 10 mA/cm<sup>2</sup>, depending on the choice of the metal cation, the M:ZrP molar ratio used during synthesis, and whether the metal was intercalated into, or adsorbed onto, ZrP. In general, lower overpotentials are observed for the higher M:ZrP molar ratios, ascribed to higher metal loadings. For the Fe(II):ZrP and Ni(II):ZrP catalysts, the intercalated systems consistently require higher overpotentials versus their adsorbed counterparts, e.g., by 34 mV and 88 mV, respectively, at a M:ZrP ratio of 10:1. A less pronounced difference in activity for the two types of metal-modification was observed for the cases of Fe(III):ZrP and Co(II):ZrP. Given that, in general, OER activities for the metal-adsorbed ZrP catalysts are greater than or equal to those of their metal-intercalated counterparts at the same loading, it is likely that the OER is dominated by catalysis on the outer surface of the ZrP supported metal-based systems rather than within the layers, which may be limited by mass transport.

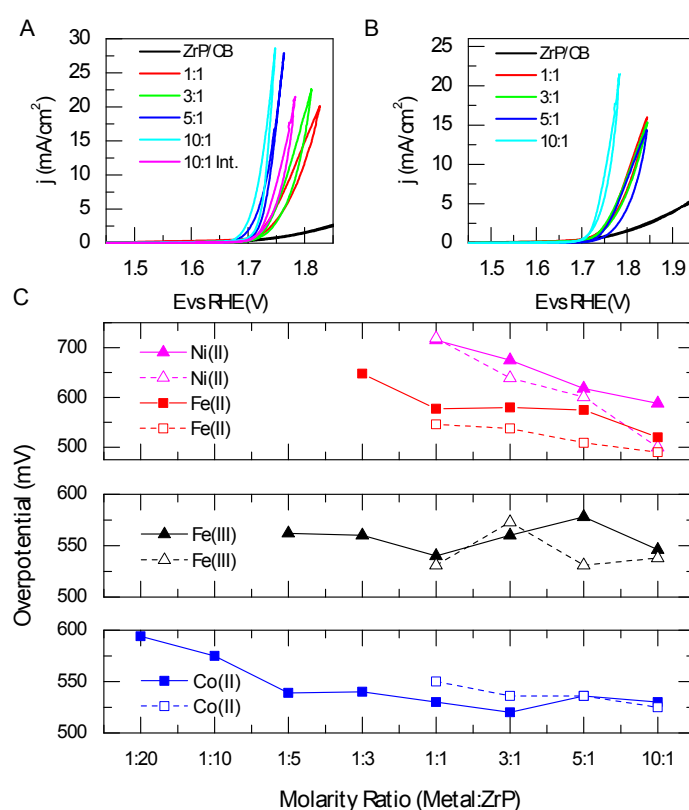


**Figure 7.** (A) Cyclic voltammograms of adsorbed Fe-ZrP. The best CV for intercalated Fe(II)-ZrP is shown in pink. (B) Cyclic voltammograms of intercalated Fe-ZrP. (C) Electrochemical performance comparison of all four metal systems for adsorbed and intercalated species at 10 mA/cm<sup>2</sup>, except for Ni(II), which was compared at 3 mA/cm<sup>2</sup>. Solid and dashed lines represent intercalated and adsorbed metal ZrP systems, respectively

While at this stage the mechanism of OER catalysis remains unclear for either the metal-intercalated ZrP or the metal-adsorbed ZrP, a further question involves conductivity, as the intercalation of metals within the interlayers could affect the conductivity of the ZrP nanoparticle [56]. Furthermore, all systems, apart from Ni(II), exhibited diminishing stability with continued cycling (Figure S4). Further work is aimed at enhancing the conductivity of the ZrP supports and tailoring the surface and interlayer properties to improve stability.

### 3. Conclusion

Our findings indicate that ZrP can serve as a support for transition metal-based OER catalysts. Increasing the M:ZrP molar ratio had a direct increase in metal content observed by XPS which correlated to an increase in activity for all metal systems. Consequently, as observed by electrochemical cyclic voltammetry, the metal species that were supported within ZrP required similar, or higher, overpotentials to drive the OER when compared to their metal-adsorbed counterparts. This may result from differences in mass transport and/or electronic conductivity in the two systems. This report on metal-modified ZrP catalysts serves as a basis for developing improved OER catalyst systems, paving the way for future work investigating various metal combinations or molecular species supported onto, or into, ZrP for enhanced catalytic activity and stability.

### 4. Materials and Methods

#### 4.1. Materials

All chemicals were obtained from commercial sources as analytical or reagent grade and used as received. Zirconium oxychloride octahydrate ( $\text{ZrOCl}_2 \cdot 8\text{H}_2\text{O}$ , 98%), iron chloride tetrahydrate ( $\text{FeCl}_2 \cdot 4\text{H}_2\text{O}$ , 98%), iron nitrate nonahydrate ( $\text{Fe}(\text{NO}_3)_3 \cdot 9\text{H}_2\text{O}$ , 98%), cobalt nitrate hexahydrate ( $\text{Co}(\text{NO}_3)_2 \cdot 6\text{H}_2\text{O}$ , 98%), nickel nitrate hexahydrate ( $\text{Ni}(\text{NO}_3)_2 \cdot 6\text{H}_2\text{O}$ , 98.5%), and Nafion<sup>®</sup> 117 (5%) were obtained from Sigma-Aldrich (St. Louis, MO, USA). Phosphoric acid ( $\text{H}_3\text{PO}_4$ , 85% *v/v*) was obtained from Fisher Scientific (Hampton, NH, USA), glassy carbon rods (SigradurG, HTW Hochtemperatur-Werkstoffe GmbH, 5 mm diameter) were processed by the Stanford University crystal shop to prepare 4 mm long pieces with the top side polished to a surface root-mean-square (RMS) roughness of less than 50 nm, and carbon black was purchased from Fuel Cell Store (College Station, TX, USA, Vulcan XC-72).

#### 4.2. $\theta$ -, $\alpha$ -, and Metal-Modified ZrP Synthesis

The synthesis for  $\theta$ -ZrP was the same as reported by Kijima [57]. First, 100 mL of 6 M  $\text{H}_3\text{PO}_4$  was heated to 94 °C under constant stirring, followed by the drop-wise addition of 100 mL of 0.05 M  $\text{ZrOCl}_2 \cdot 8\text{H}_2\text{O}$  aqueous solution. The resulting mixture was refluxed with constant stirring at 94 °C for two days forming solid  $\theta$ -ZrP particles suspended in aqueous solution. The solution was centrifuged at 10,000 RPM for 20 min, followed by removing the supernatant and then washing the remaining solid with water (18.2 M $\Omega$ ·cm, Merck Millipore, Billerica, MA, USA). This process was repeated three times, resulting in a gelatinous paste material.  $\theta$ -ZrP was converted into  $\alpha$ -ZrP by allowing  $\theta$ -ZrP to dry overnight under vacuum at room temperature.  $\theta$ -ZrP was suspended in deionized water at various M:ZrP molar ratios (10:1, 5:1, 3:1, 1:1, 1:3, 1:5, 1:10, and 1:20) with constant stirring at room temperature for five days, producing a metal-intercalated ZrP catalyst at different loading levels, where “M” refers to different metal cations studied: Fe(II), Fe(III), Co(II), and Ni(II). Each respective sample was filtered and washed with water three times and set to dry in vacuum overnight. A similar procedure was followed to produce the high molarity (1:1, 3:1, 5:1, and 10:1) ratios for the metal-modified  $\alpha$ -ZrP with a residence time of one day. The samples were centrifuged and washed, as mentioned above, and all resulting powders were pulverized and sonicated to ease their dispersion in ink solutions.

#### 4.3. Physical and Chemical Characterization (TEM, FTIR, TGA, XRPD, XPS)

Transmission electron microscopy (TEM) was performed by a FEI Tecnai (Thermo Fisher Scientific, Inc. (Waltham, MA, USA)) operated at 200 kV. Vibrational spectroscopy data was collected from 4000 to 650  $\text{cm}^{-1}$  using a Thermo Fisher Scientific, Inc. (Waltham, MA, USA) Nicolet iS50 FT-IR continuum microscope. Before analysis, the samples were prepared in the following manner: for each sample, a 2  $\mu\text{L}$  aqueous suspension was drop-casted onto an International Crystal Laboratories (Garfield, NJ, USA) Real Crystal<sup>®</sup> KBr IR card. Samples were dried on the IR card with argon gas for ca. 2 min. Thermogravimetric experiments (TGA Q500 TA Instruments, New Castle, DE, USA) were performed

at a ramp rate of  $5\text{ }^{\circ}\text{C min}^{-1}$  under a flow of 90 mL/min air and 10 mL/min nitrogen up to  $1000\text{ }^{\circ}\text{C}$ . The lattice spacing and crystallinity of the catalysts were investigated using X-ray powder diffraction (Philips PANanalytical, Almelo, The Netherlands, X'Pert Pro) with Cu  $K\alpha$  radiation ( $\lambda = 1.54184\text{ \AA}$ ). The interlayer distance of the intercalated products was obtained from Bragg's Law ( $n\lambda = 2d_{hkl} \sin \theta$ ) using the angle at which the first-order diffraction peak appears in the diffractograms, where  $\lambda$  is the wavelength of the X-ray source,  $d_{hkl}$  is the interlayer distance between planes in the unit cell and  $\theta$  is the diffraction angle. The chemical state and atomic concentration of M and Zr were examined using high-resolution XPS (PHI 5000 VersaProbe, Physical Electronics, Enzo, Chigasaki, Japan) with an Al  $K\alpha$  source. All spectra were calibrated to the adventitious carbon 1s peak at 284.8 eV and fitted using a Shirley background and constraints for doublets, such as full width at half maximum, peak areas, and peak splitting, were taken into consideration for each respective transition metal and nonmetal. Atomic concentrations were calculated using the relative peak area ratio of the Zr 3d peak and the metal 2p peak. Assuming a Poisson distribution for the noise in the data, the pooled standard deviation for each peak area which were converted to atomic concentrations were calculated by implementing a Monte Carlo simulation through CasaXPS (Casa Software Ltd., Teignmouth, Devon, UK).

#### 4.4. Ink Preparation and Electrochemical Measurements

Each catalyst ink was prepared by dispersing 2.5 mg of carbon black (Vulcan XC-72, Fuel Cell Store, College Station, TX, USA) and 5 mg of metal-modified ZrP catalyst into 1.53 mL of water, 1.02 mL of isopropanol, and 10.02  $\mu\text{L}$  of Nafion 117. Carbon black was added to create a conductive surface since ZrP is not very conductive by itself. The resulting ink was sonicated for 60 min, or longer, until it was well dispersed. Each catalyst sample was produced by placing a clean, mirror finish-polished, 5 mm diameter glassy carbon disk into a Teflon holder and mounted into an RDE apparatus (Pine Research Instrumentation, Durham, NC, USA). The RDE was inverted and 10  $\mu\text{L}$  of catalyst ink was drop-cast onto the disk which was then rotated at 600 RPM for 20–30 min until the catalyst ink dried. The metal-ZrP loading on the  $0.196\text{ cm}^2$  disk was  $0.1\text{ mg/cm}^2$ .

The OER activity of the metal-modified ZrP-based catalyst was examined using a three-electrode RDE setup. The working electrode was composed of a thin coating of catalyst on a glassy carbon disk, prepared as described above, a Pt wire counter electrode, and an Ag/AgCl reference electrode. The OER activity was determined by cycling the potential between 1.1 and 1.8 V versus the reversible hydrogen electrode (RHE) at  $20\text{ mVs}^{-1}$  in  $\text{O}_2$ -saturated 0.1 M KOH electrolyte and an electrode rotation speed of 1600 RPM. The scan rate was slow enough to ensure steady-state behavior at the electrode surface and the rotation speed was fast enough to help in product removal from the surface and limit the bubble formation from oxygen evolution. The solution resistance of the cell was measured at 100 kHz and ohmic correction occurred after testing. The typical measured solution resistance was  $\sim 45\ \Omega$ .

**Supplementary Materials:** The following are available online at [www.mdpi.com/2073-4344/7/5/132/s1](http://www.mdpi.com/2073-4344/7/5/132/s1), Figure S1: FTIR spectra for adsorbed Fe(III) at a 10:1 M:ZrP ratio; Figure S2: XRPD patterns for Fe(II), Fe(III), Co(II), and Ni(II)-intercalated ZrP at (from top to bottom) 10:1, 5:1, 3:1, 1:1, 1:3, 1:5, 1:10, and 1:20 M:ZrP molar ratios. The bottom diffraction pattern in all frames is that of pure  $\alpha$ -ZrP; Figure S3: XRPD patterns for Fe(II), Fe(III), Co(II), and Ni(II)-adsorbed ZrP systems at (from top to bottom) 10:1, 5:1, 3:1, and 1:1 M:ZrP molar ratios. The bottom diffraction pattern in all frames is that of pure  $\alpha$ -ZrP; Figure S4: Cyclic voltammograms of adsorbed Fe(II), Fe(III), Co(II), and Ni(II)-ZrP systems. The best intercalated 10:1 M:ZrP CV is shown in pink. Dashed lines represent cyclic voltammograms after 20 cycles.

**Acknowledgments:** This work was supported by the NSF under NSF Center for Chemical Innovation CHE-1305124 for Solar Fuels. J.S. was supported by the Department of Defense (DoD) through the National Defense Science and Engineering Graduate Fellowship (NDSEG) Program. Part of this work was performed at the Stanford Nano Shared Facilities (SNSF), supported by the National Science Foundation under award ECCS-1542152. The authors would like to acknowledge Alaina L. Strickler for the TEM micrographs and the Molecular Sciences Research Center of the University of Puerto Rico.

**Author Contributions:** T.F.J., J.L.C., M.V.R.-G., and J.S. conceived and designed the experiments; J.S. and M.V.R.-G. performed the experiments; J.S., I.N., and M.V.R.-G. analyzed the data; and all authors contributed in writing the paper.

**Conflicts of Interest:** The authors declare no conflict of interest.

## References

1. Ursua, A.; Gandia, L.M.; Sanchis, P. Hydrogen production from water electrolysis: Current status and future trends. *Proc. IEEE* **2012**, *100*, 410–426. [[CrossRef](#)]
2. Gahleitner, G. Hydrogen from renewable electricity: An international review of power-to-gas pilot plants for stationary applications. *Int. J. Hydrogen Energy* **2013**, *38*, 2039–2061. [[CrossRef](#)]
3. Ehteshami, S.M.M.; Chan, S.H. The role of hydrogen and fuel cells to store renewable energy in the future energy network—Potentials and challenges. *Energy Policy* **2014**, *73*, 103–109. [[CrossRef](#)]
4. Lewis, N.S.; Nocera, D.G. Powering the planet: Chemical challenges in solar energy utilization. *Proc. Natl. Acad. Sci. USA* **2006**, *103*, 15729–15735. [[CrossRef](#)] [[PubMed](#)]
5. Gray, H.B. Powering the planet with solar fuel. *Nat. Chem.* **2009**, *1*, 7. [[CrossRef](#)] [[PubMed](#)]
6. Thomsen, J.M.; Huang, D.L.; Crabtree, R.H.; Brudvig, G.W. Iridium-based complexes for water oxidation. *Dalton Trans.* **2015**, *44*, 12452–12472. [[CrossRef](#)] [[PubMed](#)]
7. Browne, M.P.; Nolan, H.; Duesberg, G.S.; Colavita, P.E.; Lyons, M.E. G. Low-overpotential high-activity mixed manganese and ruthenium oxide electrocatalysts for oxygen evolution reaction in alkaline media. *ACS Catal.* **2016**, *6*, 2408–2415. [[CrossRef](#)]
8. Enman, L.J.; Burke, M.S.; Batchellor, A.S.; Boettcher, S.W. Effects of intentionally incorporated metal cations on the oxygen evolution electrocatalytic activity of nickel (oxy)hydroxide in alkaline media. *ACS Catal.* **2016**, *6*, 2416–2423. [[CrossRef](#)]
9. Burke, M.S.; Enman, L.J.; Batchellor, A.S.; Zou, S.; Boettcher, S.W. Oxygen evolution reaction electrocatalysis on transition metal oxides and (oxy)hydroxides: Activity trends and design principles. *Chem. Mater.* **2015**, *27*, 7549–7558. [[CrossRef](#)]
10. Burke, M.S.; Kast, M.G.; Trotochaud, L.; Smith, A.M.; Boettcher, S.W. Cobalt–iron (oxy)hydroxide oxygen evolution electrocatalysts: The role of structure and composition on activity, stability, and mechanism. *J. Am. Chem. Soc.* **2015**, *137*, 3638–3648. [[CrossRef](#)] [[PubMed](#)]
11. Galán-Mascarós, J.R. Water oxidation at electrodes modified with earth-abundant transition-metal catalysts. *ChemElectroChem* **2015**, *2*, 37–50. [[CrossRef](#)]
12. Antolini, E. Iridium as catalyst and cocatalyst for oxygen evolution/reduction in acidic polymer electrolyte membrane electrolyzers and fuel cells. *ACS Catal.* **2014**, *4*, 1426–1440. [[CrossRef](#)]
13. Fabbri, E.; Habereder, A.; Waltar, K.; Kötz, R.; Schmidt, T.J. Developments and perspectives of oxide-based catalysts for the oxygen evolution reaction. *Catal. Sci. Technol.* **2014**, *4*, 3800–3821. [[CrossRef](#)]
14. Suntivich, J.; May, K.J.; Gasteiger, H.A.; Goodenough, J.B.; Shao-Horn, Y. A Perovskite oxide optimized for oxygen evolution catalysis from molecular orbital principles. *Science* **2011**, *334*, 1383–1385. [[CrossRef](#)] [[PubMed](#)]
15. McCrory, C.C.L.; Jung, S.; Ferrer, I.M.; Chatman, S.M.; Peters, J.C.; Jaramillo, T.F. Benchmarking hydrogen evolving reaction and oxygen evolving reaction electrocatalysts for solar water splitting devices. *J. Am. Chem. Soc.* **2015**, *137*, 4347–4357. [[CrossRef](#)] [[PubMed](#)]
16. Man, I.C.; Su, H.-Y.; Calle-Vallejo, F.; Hansen, H.A.; Martínez, J.I.; Inoglu, N.G.; Kitchin, J.; Jaramillo, T.F.; Nørskov, J.K.; Rossmeisl, J. Universality in oxygen evolution electrocatalysis on oxide surfaces. *ChemCatChem* **2011**, *3*, 1159–1165. [[CrossRef](#)]
17. Weng, B.; Xu, F.; Wang, C.; Meng, W.; Grice, C.R.; Yan, Y. A layered  $\text{Na}_{1-x}\text{Ni}_y\text{Fe}_{1-y}\text{O}_2$  double oxide oxygen evolution reaction electrocatalyst for highly efficient water-splitting. *Energy Environ. Sci.* **2017**, *10*, 121–128. [[CrossRef](#)]
18. Lu, Z.; Wang, H.; Kong, D.; Yan, K.; Hsu, P.-C.; Zheng, G.; Yao, H.; Liang, Z.; Sun, X.; Cui, Y. Electrochemical tuning of layered lithium transition metal oxides for improvement of oxygen evolution reaction. *Nat. Commun.* **2014**, *5*, 4345. [[CrossRef](#)] [[PubMed](#)]
19. Doyle, A.D.; Montoya, J.H.; Vojvodic, A. Improving oxygen electrochemistry through nanoscopic confinement. *ChemCatChem* **2015**, *7*, 738–742. [[CrossRef](#)]
20. Oh, H.-S.; Nong, H.N.; Reier, T.; Bergmann, A.; Gliech, M.; Ferreira de Araújo, J.; Willinger, E.; Schlögl, R.; Teschner, D.; Strasser, P. Electrochemical catalyst–support effects and their stabilizing role for  $\text{IrO}_x$

- nanoparticle catalysts during the oxygen evolution reaction. *J. Am. Chem. Soc.* **2016**, *138*, 12552–12563. [[CrossRef](#)] [[PubMed](#)]
21. Wei Seh, Z.; Kibsgaard, J.; Dickens, C.F.; Chorkendorff, I.; Nørskov, J.K.; Jaramillo, T.F. Combining theory and experiment in electrocatalysis: Insights into materials design. *Science* **2017**, *355*. [[CrossRef](#)]
  22. Wu, Z.-S.; Yang, S.; Sun, Y.; Parvez, K.; Feng, X.; Müllen, K. 3D Nitrogen-doped graphene aerogel-supported Fe<sub>3</sub>O<sub>4</sub> nanoparticles as efficient electrocatalysts for the oxygen reduction reaction. *J. Am. Chem. Soc.* **2012**, *134*, 9082–9085. [[CrossRef](#)] [[PubMed](#)]
  23. Kou, R.; Shao, Y.; Wang, D.; Engelhard, M.H.; Kwak, J.H.; Wang, J.; Viswanathan, V.V.; Wang, C.; Lin, Y.; Wang, Y.; et al. Enhanced activity and stability of Pt catalysts on functionalized graphene sheets for electrocatalytic oxygen reduction. *Electrochem. Commun.* **2009**, *11*, 954–957. [[CrossRef](#)]
  24. Ma, T.Y.; Dai, S.; Jaroniec, M.; Qiao, S.Z. Graphitic carbon nitride nanosheet-carbon nanotube three-dimensional porous composites as high-performance oxygen evolution electrocatalysts. *Angew. Chem. Int. Ed.* **2014**, *53*, 7281–7285. [[CrossRef](#)] [[PubMed](#)]
  25. Troup, J.M.; Clearfield, A. On mechanism of ion exchange in zirconium phosphates. 20. Refinement of the crystal structure of  $\alpha$ -zirconium phosphate. *Inorg. Chem.* **1977**, *16*, 3311–3314. [[CrossRef](#)]
  26. Alberti, G.; Costantino, U.; Gupta, J.P. Crystalline insoluble acid salts of tetravalent metals—XIX: Na<sup>+</sup>-catalyzed H<sup>+</sup>-Mg<sup>2+</sup> and H<sub>4</sub><sup>+</sup>-Cs<sup>2+</sup> ion exchanges on  $\alpha$ -zirconium phosphate. *J. Inorg. Nucl. Chem.* **1974**, *36*, 2109–2114. [[CrossRef](#)]
  27. Alberti, G.; Bertrami, R.; Costantino, U. Crystalline insoluble acid salts of tetravalent metals—XXII: Effect of small amounts of Na<sup>+</sup> on the ion exchange of alkaline earth metal ions on crystalline Zr(HPO<sub>4</sub>)<sub>2</sub>·H<sub>2</sub>O. *J. Inorg. Nucl. Chem.* **1976**, *38*, 1729–1732. [[CrossRef](#)]
  28. Alberti, G.; Costantino, U. Recent progress in the intercalation chemistry of layered  $\alpha$ -zirconium phosphate and its derivatives, and future perspectives for their use in catalysis. *J. Mol. Catal.* **1984**, *27*, 235–250. [[CrossRef](#)]
  29. Marti, A.; Colón, J.L. Direct ion exchange of tris(2,2'-bipyridine)ruthenium(II) into an  $\alpha$ -zirconium phosphate framework. *Inorg. Chem.* **2003**, *42*, 2830–2832. [[CrossRef](#)] [[PubMed](#)]
  30. Alberti, G.; Costantino, U.; Gill, J.S. Crystalline insoluble acid salts of tetravalent metals—XXIII: Preparation and main ion exchange properties of highly hydrated zirconium bis monohydrogen orthophosphates. *J. Inorg. Nucl. Chem.* **1976**, *38*, 1733–1738. [[CrossRef](#)]
  31. Atienzar, P.; Victoria-Rodríguez, M.; Juanes, O.; Rodríguez-Ubis, J.C.; Brunet, E.; García, H. Layered  $\gamma$ -zirconium phosphate as novel semiconductor for dye-sensitized solar cells: Improvement of photovoltaic efficiency by intercalation of a ruthenium complex-viologen dyad. *Energy Environ. Sci.* **2011**, *4*, 4718–4726. [[CrossRef](#)]
  32. Santiago, M.B.; Delet-Flores, C.; Díaz, A.; Vélez, M.M.; Zoé-Bosques, M.; Sanakis, Y.; Colón, J.L. Layered inorganic materials as redox agents: Ferrocenium-intercalated zirconium phosphate. *Langmuir* **2007**, *23*, 7810–7817. [[CrossRef](#)] [[PubMed](#)]
  33. Santiago, M.B.; Daniel, G.A.; David, A.; Casañas, B.; Hernández, G.; Guadalupe, A.R.; Colón, J.L. Effect of enzyme and cofactor immobilization on the response of ethanol oxidation in zirconium phosphate modified biosensors. *Electroanalysis* **2010**, *22*, 1097–1105. [[CrossRef](#)]
  34. Rivera, E.J.; Barbosa, C.; Torres, R.; Grove, L.; Taylor, S.; Connick, W.B.; Clearfield, A.; Colón, J.L. Vapochromic and vapoluminescent response of materials based on platinum(ii) complexes intercalated into layered zirconium phosphate. *J. Mater. Chem.* **2011**, *21*, 15899–15902. [[CrossRef](#)]
  35. Díaz, A.; Saxena, V.; González, J.; David, A.; Casañas, B.; Carpenter, C.; Batteas, J.D.; Colón, J.L.; Clearfield, A.; Hussain, M.D. Zirconium phosphate nanoplatelets: A novel platform for drug delivery in cancer therapy. *Chem. Commun.* **2012**, *48*, 1754–1756. [[CrossRef](#)] [[PubMed](#)]
  36. Horsley, S.E.; Nowell, D.V.; Stewart, D.T. The infrared and Raman spectra of  $\alpha$ -zirconium phosphate. *Spectrochim. Acta Part A Mol. Spectrosc.* **1974**, *30*, 535–541. [[CrossRef](#)]
  37. Mosby, B.M.; Díaz, A.; Bakhmutov, V.; Clearfield, A. Surface functionalization of zirconium phosphate nanoplatelets for the design of polymer fillers. *ACS Appl. Mater. Interfaces* **2014**, *6*, 585–592. [[CrossRef](#)] [[PubMed](#)]
  38. Szirtes, L.; Szeleczky, A.M.; Rajeh, A.O.; Kuzmann, E. Thermal behaviour of transition metal-containing zirconium phosphate. *J. Therm. Anal. Calorim.* **1999**, *56*, 447–451. [[CrossRef](#)]

39. Alberti, G.; Casciola, M.; Costantino, U.; Vivani, R. Layered and pillared metal(IV) phosphates and phosphonates. *Adv. Mater.* **1996**, *8*, 291–303. [CrossRef]
40. Alagna, L.; Prospero, T.; Tomlinson, A.A.G.; Ferragina, C.; La Ginestra, A. Extended X-ray absorption fine structure investigation of local symmetry changes in Co<sup>2+</sup>- and Ni<sup>2+</sup>-exchanged zirconium phosphates. *J. Chem. Soc. Faraday Trans. 1 Phys. Chem. Condens. Ph.* **1983**, *79*, 1039–1047. [CrossRef]
41. Alagna, L.; Tomlinson, A.A.G.; Ferragina, C.; La Ginestra, A. Zirconium phosphates partially exchanged with transition-metal ions: Characterisation and stereochemical changes induced by heat treatment. *J. Chem. Soc. Dalton Trans.* **1981**, 2376–2384. [CrossRef]
42. Mani, B.; de Neufville, J.P. Dehydration of chemically and electrochemically impregnated (CI and EI) nickel hydroxide electrodes. *J. Electrochem. Soc.* **1988**, *135*, 800–803. [CrossRef]
43. Miessler, G.L.; Fischer, P.J.; Tarr, D.A. *Inorganic Chemistry*, 5th ed.; Pearson Education: London, UK, 2014; pp. 374–377.
44. Casañas-Montes, B.; Díaz, A.; Barbosa, C.; Ramos, C.; Collazo, C.; Meléndez, E.; Queffelec, C.; Fayon, F.; Clearfield, A.; Bujoli, B.; et al. Molybdocene dichloride intercalation into zirconium phosphate nanoparticles. *J. Organomet. Chem.* **2015**, *791*, 34–40. [CrossRef]
45. Sun, L.; Boo, W.J.; Sue, H.-J.; Clearfield, A. Preparation of  $\alpha$ -zirconium phosphate nanoplatelets with wide variations in aspect ratios. *New J. Chem.* **2007**, *31*, 39–43. [CrossRef]
46. Costantino, U.; Szirtes, L.; Kuzmann, E.; Megyeri, J.; Lázár, K. Exchange of iron ions into layers of  $\alpha$ -zirconium phosphate. *Solid State Ion.* **2001**, *141*, 359–364. [CrossRef]
47. Yamashita, T.; Hayes, P. Analysis of XPS spectra of Fe<sup>2+</sup> and Fe<sup>3+</sup> ions in oxide materials. *Appl. Surf. Sci.* **2008**, *254*, 2441–2449. [CrossRef]
48. Nemoskhalenko, V.V.; Didyk, V.V.; Krivitskii, V.P.; Senekevich, A.I. Investigation of the atomic charges in iron, cobalt and nickel phosphides. *Zhurnal Neorganicheskoi Khimii* **1983**, *28*, 2182–2192.
49. Hernández-Huesca, R.; Braos-García, P.; Mérida-Robles, J.; Maireles-Torres, P.; Rodríguez-Castellón, E.; Jiménez-López, A. Cobalt-based alumina pillared zirconium phosphate catalysts for the selective catalytic reduction of NO by propane. *Chemosphere* **2002**, *48*, 467–474. [CrossRef]
50. Nardi, K.L.; Yang, N.; Dickens, C.F.; Strickler, A.L.; Bent, S.F. Creating highly active atomic layer deposited NiO electrocatalysts for the oxygen evolution reaction. *Adv. Energy Mater.* **2015**, *5*, 1500412. [CrossRef]
51. Cheikhi, N.; Ziyad, M. Methane conversion to higher alkanes over ruthenium and cobalt loaded Zr<sub>3</sub>(PO<sub>4</sub>)<sub>4</sub>. *J. Phys. IV* **2005**, *123*, 301–305. [CrossRef]
52. Zhan, Y.; Lu, M.; Yang, S.; Liu, Z.; Lee, J.Y. The origin of catalytic activity of nickel phosphate for oxygen evolution in alkaline solution and its further enhancement by iron substitution. *ChemElectroChem* **2016**, *3*, 615–621. [CrossRef]
53. Colón, J.L.; Thakur, D.S.; Yang, C.-Y.; Clearfield, A.; Martin, C.R. X-ray photoelectron spectroscopy and catalytic activity of  $\alpha$ -zirconium phosphate and zirconium phosphate sulfophenylphosphonate. *J. Catal.* **1990**, *124*, 148–159. [CrossRef]
54. Arfelli, M.; Mattogno, G.; Ferragina, C.; Massucci, M.A. XPS characterization of  $\gamma$ -zirconium phosphate and of some of its intercalation compounds. A comparison with the  $\alpha$ -zirconium phosphate analogues. *J. Incl. Phenom. Mol. Recognit. Chem.* **1991**, *11*, 15–27. [CrossRef]
55. Xie, J.; Wang, R.; Bao, J.; Zhang, X.; Zhang, H.; Li, S.; Xie, Y. Zirconium trisulfide ultrathin nanosheets as efficient catalysts for water oxidation in both alkaline and neutral solutions. *Inorg. Chem. Front.* **2014**, *1*, 751–756. [CrossRef]
56. Szirtes, L.; Megyeri, J.; Kuzmann, E.; Klencsár, Z. Electrical conductivity of transition metal containing crystalline zirconium phosphate materials. *Solid State Ion.* **2001**, *145*, 257–260. [CrossRef]
57. Kijima, T. Direct preparation of  $\theta$ -zirconium phosphate. *Bull. Chem. Soc. Jpn.* **1982**, *55*, 3031–3032. [CrossRef]

